

The magnetic, spectroscopic, and photometric variability of the Wolf-Rayet star WR 55

S. P. Järvinen¹, S. Hubrig¹, R. Jayaraman², A. Cikota³, M. Schöller⁴

¹Leibniz-Institut für Astrophysik Potsdam (AIP), An der Sternwarte 16, 14482 Potsdam, Germany

²MIT Kavli Institute and Department of Physics, 77 Massachusetts Avenue, Cambridge, MA 02139, USA

³Gemini Observatory / NSF's NOIRLab, Casilla 603, La Serena, Chile

⁴European Southern Observatory, Karl-Schwarzschild-Str. 2, 85748 Garching, Germany

Accepted 2023 June 02. Received 2023 May 22; in original form 2023 April 06

ABSTRACT

Studies of magnetic fields in the most evolved massive stars, the Wolf-Rayet stars, are of special importance because they are progenitors of certain types of supernovae. The first detection of a magnetic field of the order of a few hundred Gauss in the WN7 star WR 55, based on a few FORS 2 low-resolution spectropolarimetric observations, was reported in 2020. In this work we present new FORS 2 observations allowing us to detect magnetic and spectroscopic variability with a period of 11.90 h. No significant frequencies were detected in TESS and ASAS-SN photometric observations. Importantly, magnetic field detections are achieved currently only in two Wolf-Rayet stars, WR 6 and WR 55, both showing the presence of corotating interacting regions.

Key words: techniques: polarimetric — techniques: spectroscopic — techniques: photometric — stars: individual: WR 55 — stars: magnetic field — stars: Wolf-Rayet

1 INTRODUCTION

The role of magnetic fields in the evolution of massive stars remains poorly understood. Massive O stars have been found to have large-scale organized, predominantly dipolar magnetic fields (e.g., Hubrig et al. 2013; Grunhut et al. 2017; Schöller et al. 2017; Hubrig et al. 2023), so that we expect to detect such fields in their descendants, the Wolf-Rayet (WR) stars. Aguilera-Dena et al. (2020) calculated a sequence of rotating, magnetized pre-collapse models for WR stars with sub-solar metallicity and suggested that the presence of magnetic fields could explain extreme events such as superluminous supernovae and gamma-ray bursts powered by proto-magnetars or collapsars. They concluded that further modelling of WR stars with different metallicities and rotational velocities will allow for comparisons with observed rates of superluminous supernovae and gamma-ray bursts.

Gayley & Ignace (2010) predicted a fractional circular polarization of a few times 10^{-4} for WR magnetic fields of about 100 G. Verifying this prediction observationally, however, is difficult due to the WR stars' significantly broadened emission-line spectra arising from a strong stellar wind. Recent work has found evidence for WR magnetic fields: marginal detections in three stars by de la Chevrotière et al. (2014), who used high-resolution spectropolarimetry, and a 3.3σ detection of a mean longitudinal magnetic field $\langle B_z \rangle$ in the cyclically variable, X-ray emitting WN5-type star WR 6 by Hubrig et al. (2016), who used low-resolution FORS 2 spectropolarimetry (Appenzeller et al. 1998). Cyclical vari-

ability can arise from a corotating interacting region (CIR), whose signatures include different photospheric absorption features simultaneously propagating with different accelerations. CIRs in massive stars have been found using spectroscopic time series (e.g., Mullan 1984). These may relate to magnetic bright spots, which often signal the presence of a global magnetic field (e.g., Ramiaramanantsoa et al. 2014).

Hubrig et al. (2020) reported a definite detection in another WR star with similar cyclical variability (Chené & St-Louis 2011), the hydrogen-deficient WN7-type star WR 55 ($T_{\text{eff}} = 56.2$ kK; Hamann, Gräfener & Liermann 2006). The measured $\langle B_z \rangle$ showed a change in polarity, with the highest field values $\langle B_z \rangle = -378 \pm 85$ G (4.4σ) and $\langle B_z \rangle = 205 \pm 58$ G (3.5σ). This work presents additional FORS 2 spectropolarimetric observations of WR 55, alongside photometry, and aims to constrain the magnetic field strength and identify any periodicities.

2 MAGNETIC AND SPECTRAL VARIABILITY

Twelve new FORS 2 spectropolarimetric observations, in addition to the four observations presented in Hubrig et al. (2020), are listed in Table 1. The new spectra were acquired between 2022 February 16 and April 11, with the same instrument setup as in Hubrig et al. (2020). The wavelength was calibrated with a He-Ne-Ar arc lamp, and the extraction of the ordinary and extraordinary beams was done using

Table 1. Longitudinal magnetic field values $\langle B_z \rangle$ of WR 55 from FORS 2 spectropolarimetric observations. The first column gives the modified Julian date (MJD) of mid-exposure, followed by the corresponding rotational phase for a period of 11.90 h and $T_0 = 59664.226$, and then the values for the signal-to-noise ratio (S/N) of the Stokes I spectra measured near 4686 Å. The last two columns show the $\langle B_z \rangle$ measurements from the Monte Carlo bootstrapping test, and the corresponding measurements $\langle N_z \rangle$ from the null spectra. Errors represent 1σ uncertainties. Observations with * are from Hubrig et al. (2020).

MJD	φ	S/N	$\langle B_z \rangle$ G	$\langle N_z \rangle$ (G)
58892.2058*	0.067	2388	205±58	-16±55
58898.3492*	0.457	2579	-378±85	-6±78
58900.2075*	0.204	2168	56±80	63±82
58916.3059*	0.670	2386	4±66	-16±57
59627.2359	0.401	3402	-172±47	-26±45
59652.2534	0.854	2618	143±81	29±79
59660.0977	0.674	2726	-47±49	-37±48
59662.3518	0.219	3057	-73±38	-16±41
59664.3504	0.250	3073	-33±34	18±31
59666.3152	0.212	2822	-35±55	20±46
59667.2918	0.182	3082	-129±42	-13±46
59668.3296	0.275	2599	-44±52	38±46
59670.0844	0.814	2710	114±48	-19±49
59671.2429	0.152	2755	81±47	-25±48
59679.2081	0.213	2818	-26±43	-24±42
59681.0112	0.850	2455	156±53	54±55

standard IRAF procedures (Cikota et al. 2017). The measurements of the mean longitudinal magnetic field were carried out using procedures presented in prior work (e.g., Hubrig et al. 2004a,b; Schöller et al. 2017, and references therein).

Our frequency analysis based on the $\langle B_z \rangle$ measurements in Table 1 was performed using a Levenberg-Marquadt non-linear least-squares fit (Press et al. 1992). To detect the most probable period, we calculated the frequency spectrum, and for each trial frequency, we performed a statistical F-test of the null hypothesis – the absence of periodicity (Seber 1977). The resulting F-statistic can be thought of as the total sum, including covariances, of the ratio of harmonic amplitudes to their standard deviations, i.e., a S/N. As shown in the top panel of Fig. 1, the highest peak in the frequency spectrum corresponds to a period $P = 11.9006 \pm 0.0001$ h. The distribution of the measured $\langle B_z \rangle$ values over this period assuming the ephemeris $T_0 = 59664.2260$ is presented in the bottom panel of Fig. 1. Assuming a dipolar field structure, this ephemeris corresponds to the maximum positive field extremum in the corresponding sinusoidal field phase curve.

Additionally, three spectral lines, the He II and H β blend, the He II 5412 Å line, and the C IV doublet were investigated for the presence of rotationally-modulated variability of line intensities and radial velocities. The results of the frequency analysis of equivalent widths (EWs) for all three lines are presented in the top panel of Fig. 2. The highest peaks in the frequency spectra not coinciding with the window function correspond to slightly longer periods: $P = 11.95 \pm 0.0020$ h for the He II/H β blend, and $P = 11.94 \pm 0.0002$ h for the He II and C IV lines. Notably, our frequency analysis indicates a lower significance for the periods obtained using EWs than for the period using the

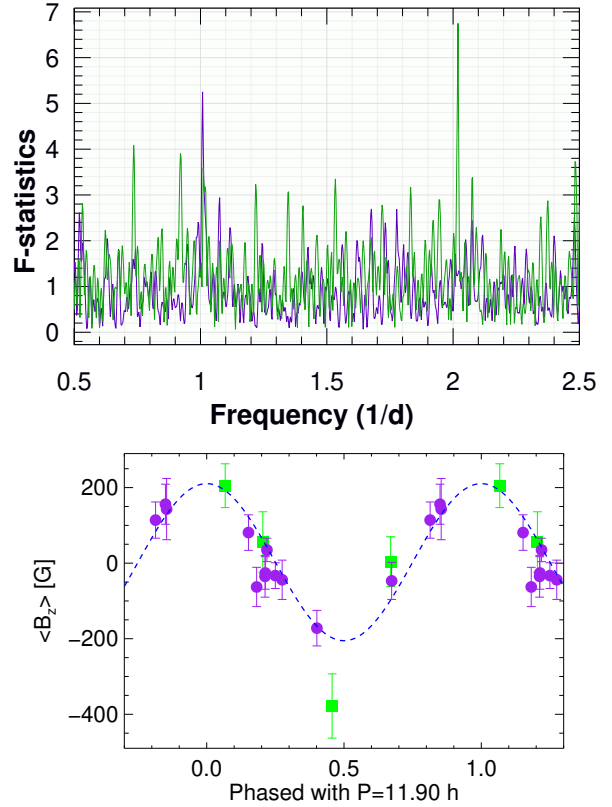


Figure 1. *Top:* F-statistics periodogram (green) for the $\langle B_z \rangle$ measurements of WR 55, with the window function (purple). *Bottom:* $\langle B_z \rangle$ measurements of WR 55 from low-resolution FORS 2 spectropolarimetric observations, phased with the period of 11.90 h. The dashed blue curve corresponds to the sinusoidal fit. Green squares are measurements from Hubrig et al. (2020), purple dots are from 2022. Vertical bars indicate the measurement accuracy.

magnetic field measurements directly: the reduced χ^2 -values for the fits are 1.10 for the $\langle B_z \rangle$ measurements, 5.83 for the He II/H β blend, 15.00 for the He II 5412 Å line, and 13.30 for the C IV doublet. The distributions of the EW values over the detected periods, assuming the same ephemeris as for the magnetic field measurements, are presented in the bottom panel of Fig. 2. We observe a clear phase shift of 0.22 between the maxima of the measured EW and the magnetic maximum. As WR 55 is a CIR-type variable target, a curvature due to a spiral CIR can result in the development of a potentially exploitable phase lag (Ignace, St-Louis & Prinza 2020).

Variability of EWs can be caused either by an inhomogeneous distribution of temperature or chemical elements on the surface of a rotating star, or a companion. Concerning the last possibility, we find no information in the literature on the binarity of WR 55. We do not detect any significant frequency peaks in our measurements of the radial velocities. This may be because the emission-line spectra of WR stars are mainly formed in expanding atmospheric layers, where the wavelength and shapes of emission lines have multiple contributions: from wind velocity, stellar rotation, and (potential) orbital motion. Because CIRs may be explained via a paradigm involving bright spots driving CIR structures, we assume that the observed EW variability can be explained by temperature spots. The individual lines used in the equiv-

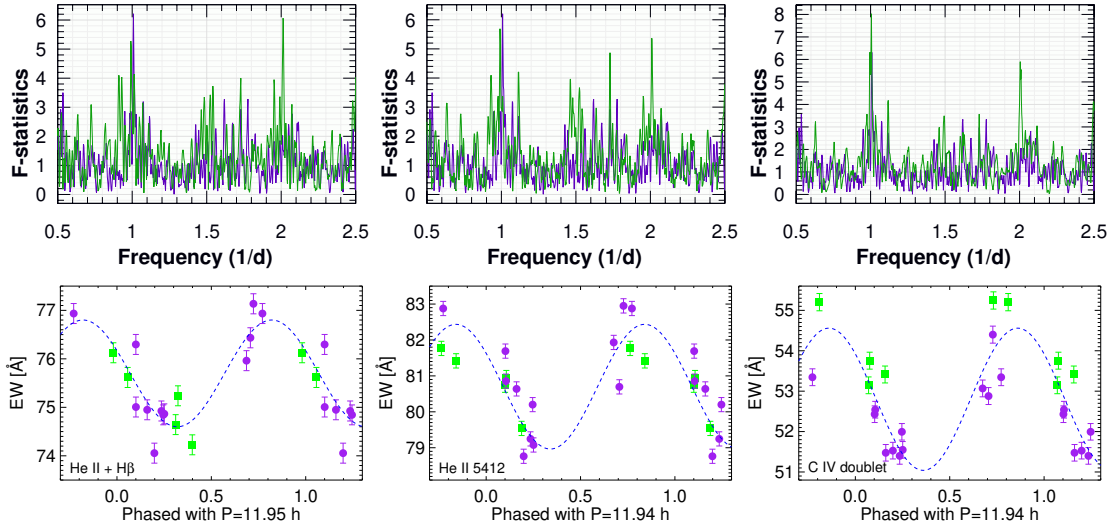


Figure 2. *Top:* F-statistics periodogram (green) for equivalent widths of the He II and H β blend (left), the He II 5412 Å line (middle), and the C IV doublet (right). *Bottom:* The corresponding phase curves, with symbols as in Fig. 1. Vertical bars show measurement accuracy.

alent widths measurements are most likely formed slightly higher up in the expanding atmosphere (we estimate by 0.3% of the stellar radius), so that the rotation period becomes longer due to the conservation of angular momentum.

3 PHOTOMETRIC VARIABILITY

3.1 TESS photometry and contamination

WR 55 was observed by TESS in Sectors 11 and 38, from 2019 April 22 to 2019 May 21, and from 2021 April 28 to 2021 May 26. We constructed custom light curves for Sector 11 with `TESSCut` (Brasseur et al. 2019), and for Sector 38 from the Target Pixel File (TPF) output by the Science Processing Operations Center (SPOC) pipeline (Jenkins et al. 2016), using `lightkurve` (Lightkurve Collaboration 2018).

TESS light curves often suffer significant contamination from nearby stars due to the large plate scale (21"/pixel). For WR 55, there is a nearby bright ($G_{\text{RP}} = 8.63$) β Cephei variable star (HD 117704) whose flux could fall into the chosen aperture. Figure 3 shows the magnitudes (in G_{RP} band, which spans a similar range as the TESS passband) and locations of bright ($G_{\text{RP}} < 13$) sources near WR 55, from Gaia Data Release 3 (Gaia Collaboration 2016, 2021). To mitigate possible contamination, we used a custom one-pixel aperture including only WR 55 (light green shading in the left panel of Fig. 3; purple shading corresponds to the SPOC aperture). The 30-minute cadence light curve from Sector 11 was extracted via `TESSCut` using a similar one-pixel aperture; backgrounds were estimated as in section 2 of Toalá et al. (2022). These light curves did not need detrending. The light curves and periodograms of Sectors 11 and 38 are similar.

3.2 The Low-Frequency Excess

We used the Discrete Fourier Transform (Deeming 1975) to calculate the periodograms of the light curves. Bowman et al. (2019a,b), Nazé, Rauw & Gosset (2021), and Lenoir-Craig et al. (2022) assign a physical interpretation to the

low-frequency excess (red noise) in the frequency spectra of massive stars. For WR stars in particular, three explanations have been posited: (a) interactions between clumped stellar wind and pulsations (Nazé, Rauw & Gosset 2021), (b) internal gravity waves (Bowman et al. 2019b), and (c) a sub-surface convection zone caused by an iron-peak opacity bump (“FeCZ”; see, e.g., Cantiello et al. 2009), which is most pronounced in WR stars. Lenoir-Craig et al. (2022) also suggest a line-deshadowing instability (LDI) to explain the variability. Finally, CIRs can also induce flux variability, but this was studied only in the radio (Ignace, St-Louis & Prinja 2020).

As in prior literature, we fit the red noise with a semi-Lorentzian function added to a white noise term:

$$A(\nu) = \frac{A_0}{1 + \left(\frac{\nu}{\nu_{\text{char}}}\right)^\gamma} + C_W, \quad (1)$$

where A_0 represents the amplitude scale of the low-frequency variability, ν_{char} is its characteristic frequency, γ is an exponent, and C_W is the white noise component, which also captures instrumental variability. For our fit, we compare a custom implementation of the Markov Chain Monte Carlo (MCMC) method and the Levenberg-Marquadt non-linear least-squares method (with `lmfit`; Newville et al. 2014).

To calculate formal uncertainties in power spectra amplitudes, we first assumed a Poisson uncertainty (\sqrt{N} ; N is the count of e^- /second) for each point in both light curves and then bootstrapped 1000 realizations of these points, with Gaussian noise. We then calculated the Lomb-Scargle periodogram using `lightkurve` (Lomb 1976; Scargle 1982; Lightkurve Collaboration 2018) and then used the standard deviation of the amplitudes in each frequency bin (across all 1000 power spectra) as the formal per-point uncertainty to be used when fitting, in order to derive parameter uncertainties. We contrast this with Nazé, Rauw & Gosset (2021), wherein parameter uncertainties are the square root of the diagonal of the covariance matrix, multiplied by $\sqrt{\chi^2_{\text{best fit}}}$, divided by $0.5 \times N_{\text{data}} - 4$ (degrees of freedom).

The MCMC ran for 5×10^6 steps; priors (see Table 2)

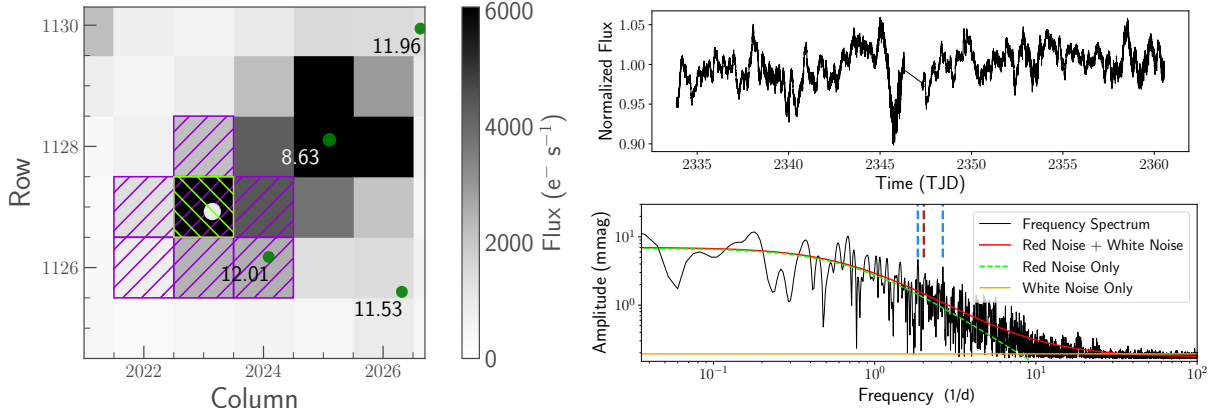


Figure 3. *Left:* The Sector 38 target pixel file of WR 55, with nearby Gaia sources ($G_{\text{RP}} < 13$) and magnitudes. WR 55 is in white; other sources are in dark green. The β Cephei star HD 117704, with $G_{\text{RP}} = 8.63$ source, is labeled in white. Purple shading represents the photometric aperture chosen by the SPOC pipeline (Jenkins et al. 2016); light green represents our chosen aperture for the custom light curve in the top right panel. *Right:* The bottom panel shows the best-fit semi-Lorentzians for the power spectrum for the light curve in the top panel, based on the parameters in Table 2. The black line is the power spectrum, while the red line represents the best-fit red + white noise model. These two are also plotted separately (light green and orange, respectively). Marginal frequencies are denoted by blue dotted lines (see further discussion in the text), while purple corresponds to the magnetic period obtained in Section 2.

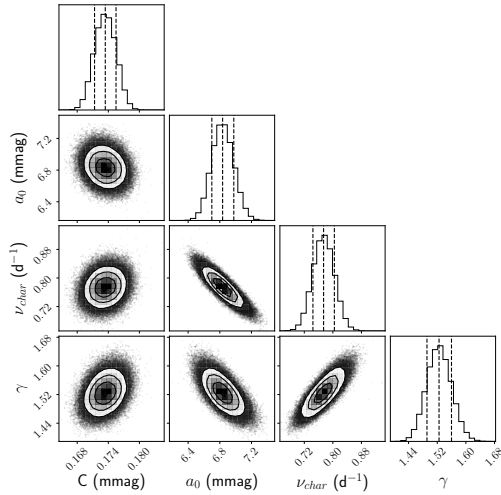


Figure 4. Posterior distributions for Sector 38 red noise parameters of WR 55. Dashed vertical lines represent the 16th, 50th, and 84th percentiles (left to right). Strong negative correlations exist for (a_0, ν_{char}) , (a_0, γ) , and a strong positive one for $(\nu_{\text{char}}, \gamma)$.

were derived iteratively, with initial estimates based on the ranges of values in Nazé, Rauw & Gosset (2021) and Lenoir-Craig et al. (2022). Best-fit parameter values from both techniques are in Table 2; they agree to within their (similar) mutual uncertainties. Posterior distributions for Sector 38 parameters are in Fig. 4. This is the first application and comparison of both techniques for the same star, showing that they are equally valid; Lenoir-Craig et al. (2022) solely used MCMC, while Nazé, Rauw & Gosset (2021) used only Levenberg-Marquadt. The best-fit semi-Lorentzians are shown in Fig. 3; an F-test shows that a red noise model is strongly favored over a white-noise-only model ($p < 10^{-16}$).

3.3 Photometric Peaks

No significant ($S/N > 5$) or marginal ($3 < S/N < 5$) peaks were found in Sector 11. In Sector 38, we find two marginal peaks at $1.8544 \pm 0.0003 \text{ d}^{-1}$ and $2.6485 \pm 0.0003 \text{ d}^{-1}$ (blue dashed lines in Fig. 3). To search for longer-period variability, we used the light curve from the All-Sky Automated Survey for Supernovae Sky Patrol web server (Kochanek et al. 2017, with a Nyquist limit of $\sim 0.5 \text{ d}$). Data were separated by camera, and the periodograms were calculated with *astropy* (Astropy Collaboration 2013). We found marginal peaks at $\sim 6.4 \text{ d}$ (in camera *be*) and $\sim 20\text{--}25 \text{ d}^{-1}$ (in both cameras); we do not ascribe physical meaning to these.

None of these periods matches $P = 11.9 \text{ h}$ from Sect. 2 (the brown dashed line in the bottom right panel of Fig. 3), or the observed pulsation frequencies of the nearby β Cep star. Marginal peaks may correspond to pulsation modes, which shift, appear, and disappear over many months, and may underlie the discrepancy in red noise parameters between sectors. Recovery of WR 55’s photometric rotation period may also be hindered by circumstellar material.

4 DISCUSSION AND CONCLUSIONS

Hubrig et al. (2020) found a magnetic field in WR 55, and our additional observations confirm this and constrain the $\langle B_z \rangle$ amplitude to $\sim 200 \text{ G}$. The sinusoidal field phase curve indicates a likely dipolar field structure. After the detection of a longitudinal magnetic field in WR 6, WR 55 is now the second magnetic star showing the presence of a CIR, suggesting that WRs with CIRs are good candidates for future magnetic surveys.

Notably, pulsations cannot cause the short periodicity in WR 55, as we see a change in field polarity. While low-amplitude magnetic variability has been found in pulsating magnetic stars, these changes in $\langle B_z \rangle$ are $\sim 10\text{--}15 \text{ G}$ (e.g., Shultz et al. 2017). Similar short periodicities have been reported for other stars (e.g., 9.8 h in WR 123, Chené et al.

Table 2. Best-fit parameters and uncertainties from both fitting methods for all data for WR 55, along with MCMC priors.

Parameter	MCMC				Least-Squares	
	Sec. 11	Sec. 11 Prior	Sec. 38	Sec. 38 Prior	Sec. 11	Sec. 38
C_W (mmag)	0.697 ± 0.012	$0.6 \leq C_W \leq 0.8$	0.173 ± 0.002	$0.15 \leq C_W \leq 0.2$	0.697 ± 0.014	0.173 ± 0.001
A_0 (mmag)	10.9 ± 0.2	$10 \leq A_0 \leq 13$	6.84 ± 0.14	$5 \leq A_0 \leq 8$	11.0 ± 0.3	6.84 ± 0.04
ν_{char} (d ⁻¹)	0.300 ± 0.012	$0.25 \leq \nu_{\text{char}} \leq 0.35$	0.774 ± 0.030	$0.6 \leq \nu_{\text{char}} \leq 1.0$	0.300 ± 0.014	0.772 ± 0.007
γ	1.39 ± 0.03	$1.25 \leq \gamma \leq 1.5$	$1.53^{+0.04}_{-0.03}$	$1.25 \leq \gamma \leq 1.75$	1.38 ± 0.04	1.52 ± 0.01

2011; 15.5 h in WR 46, Hénault-Brunet et al. 2011). With our period and a radius estimate of $5.23R_{\odot}$ from Hamann et al. (2019), we find $v_{\text{eq}} = 534 \text{ km s}^{-1}$, suggesting that WR 55 was perhaps spun up by binary interaction (de Mink et al. 2012). Magnetic spectropolarimetry of WR stars, especially nitrogen-sequence WN stars, is crucial, as they are likely progenitors of type Ib or IIb supernovae (Stevance 2019).

Finally, we compare our photometric results for WR 55 with the large samples of Nazé, Rauw & Gosset (2021) and Lenoir-Craig et al. (2022). Table 2 of Lenoir-Craig et al. (2022) shows their best-fit values of the four semi-Lorentzian parameters; we focus on WR 78 and WR 87, which are like WR 55: WN-type stars with both 30- and 2-minute cadence data. These two stars have A_0 and C_W decreasing between sectors, but ν_{char} and γ increase, which agrees with our findings for WR 55. This effect (especially for A_0 and C_W) may partially arise from the differing cadences and noise properties of the data; this is explored in fig. 5 of Lenoir-Craig et al. (2022). However, γ (and ν_{char}) correspond to intrinsic properties of the star, so their change across sectors is interesting and may indicate the existence of slow, internal stellar processes. For instance, both our values of γ agree with the predictions of Edelmann et al. (2019) and may indicate core-generated internal gravity waves. More data will help untangle the relative effects of sources of flux variability.

ACKNOWLEDGEMENTS

We thank our referee, Dr. Pascal Petit, for insightful comments. This work is based on observations made with ESO telescopes at the La Silla Paranal Observatory under programme IDs 0104.D-0246(A) and 109.230H.001. This paper includes data collected by the TESS mission. Funding for the TESS mission is provided by the NASA Science Mission Directorate. Resources supporting this work were also provided by the NASA High-End Computing (HEC) Program through the NASA Advanced Supercomputing (NAS) Division at Ames Research Center to produce the SPOC data products (Jenkins et al. 2016). The 2-min cadence data of WR 55 were obtained via Guest Investigator program G03095 (PI: T. Dorn-Wallenstein).

DATA AVAILABILITY

All FORS 2 data are available from the ESO Science Archive Facility at <http://archive.eso.org/cms.html>.

TESS data can be downloaded from the Barbara A. Mikulski Archive for Space Telescopes (mast.stsci.edu).

REFERENCES

- Aguilera-Dena D. R., Langer N., Antoniadis J., Müller B., 2020, *ApJ*, 901, 114
- Appenzeller I., et al., 1998, *The ESO Messenger*, 94, 1
- Astropy Collaboration, et al., 2013, *A&A*, 558, A33
- Bowman D. M., et al., 2019a, *Nature Astronomy*, 3, 760
- Bowman D. M., et al., 2019b, *A&A*, 621, A135
- Brasseur C. E., Phillip C., Fleming S. W., Mullally S. E., White R. L., 2019, *Astrophysics Source Code Library*, record ascl:1905.007
- Cantiello M., et al., 2009, *A&A*, 499, 279
- Chené A.-N., St-Louis N., 2011, *ApJ*, 736, 140
- Chené A.-N., et al., 2011, *A&A*, 530, A151
- de la Chevrotière A., St-Louis N., Moffat A. F. J., MiMeS Collaboration, 2014, *ApJ*, 781, 73
- Cikota A., Patat F., Cikota S., Faran T., 2017, *MNRAS*, 464, 4146
- Deeming T. J., 1975, *Ap&SS*, 36, 137
- Edelmann P. V. F., Ratnasingam R. P., Pedersen M. G., Bowman D. M., Prat V., Rogers T. M., 2019, *ApJ*, 876, 4
- Gaia Collaboration et al., 2016, *A&A*, 595, A1
- Gaia Collaboration et al., 2021, *A&A*, 649, A1
- Gayley K. G., Ignace R., 2010, *ApJ*, 708, 615
- Grunhut J. H., et al., 2017, *MNRAS*, 465, 2432
- Hamann W.-R., Gräfener G., Liermann A., 2006, *A&A*, 457, 1015
- Hamann W.-R., et al., 2019, *A&A*, 625, A57
- Hénault-Brunet V., St-Louis N., Marchenko S. V., Pollock A. M. T., Carpano S., Talavera A., 2011, *ApJ*, 735, 13
- Hubrig S., Kurtz D. W., Bagnulo S., Szeifert T., Schöller M., Mathys G., Dziembowski W. A., 2004a, *A&A*, 415, 661
- Hubrig S., Szeifert T., Schöller M., Mathys G., Kurtz D. W., 2004b, *A&A*, 415, 685
- Hubrig S., et al., 2013, *A&A*, 551, A33
- Hubrig S., et al., 2016, *MNRAS*, 458, 3381
- Hubrig S., Schöller M., Cikota A., Järvinen S. P., 2020, *MNRAS*, 499, L116
- Hubrig S., Järvinen S. P., Ilyin I., Schöller M., Jayaraman R., 2023, *MNRAS*, 521, 6228
- Ignace R., St-Louis N., Prinja R. K., 2020, *MNRAS*, 497, 1127
- Jenkins J. M., et al., 2016, in Chiozzi G., Guzman J. C., eds, *Proc. SPIE Conf. Ser. Vol. 9913*, SPIE, Bellingham, p. 99133E
- Kochanek C. S., et al., 2017, *PASP*, 129, 104502
- Lenoir-Craig G., et al., 2022, *ApJ*, 925, 79
- Lightkurve Collaboration, et al., 2018, *Astrophysics Source Code Library*, record ascl:1812.013
- Lomb N. R., 1976, *Ap&SS*, 39, 447
- de Mink S. E., Brott I., Cantiello M., Izzard R. G., Langer N., Sana H., 2012, in Drissen L., Robert C., St-Louis N., Moffat A. F. J., eds, *ASP Conf. Ser., Vol. 465*, San Francisco, p. 65
- Mullan D. J., 1984, *ApJ*, 283, 303
- Nazé Y., Rauw G., Gosset E., 2021, *MNRAS*, 502, 5038
- Newville M., Stensitzki T., Allen D. B., Ingargiola A., 2014, doi:10.5281/zenodo.11813
- Press W. H., Teukolsky S. A., Vetterling W. T., Flannery B. P., 1992, *Numerical Recipes*, 2nd edn. Cambridge: Cambridge

- University Press
Ramiaramanantsoa T., et al., 2014, MNRAS, 441, 910
Scargle J. D., 1982, ApJ, 263, 835
Schöller M., et al., 2017, A&A, 599, A66
Shultz M., Wade G. A., Rivinius Th., Neiner C., Henrichs H.,
Marcolino W., 2017, MNRAS, 471, 2286
Seber G. A. F., 1977, Linear Regression Analysis. Wiley, New
York
Stevance H. F. 2019, PhD Thesis, University of Sheffield,
arXiv:1906.07184
Toalá J. A., et al., 2022, MNRAS, 514, 2269

This paper has been typeset from a $\text{T}_{\text{E}}\text{X}/\text{L}^{\text{A}}\text{T}_{\text{E}}\text{X}$ file prepared by
the author.